A TRAJECTORY DESIGN FRAMEWORK LEVERAGING LOW-THRUST FOR THE LUNAR ICECUBE MISSION

Robert Pritchett[*], Kathleen Howell[†], and David Folta[‡]

The 6U Cubesat, Lunar IceCube (LIC), is a secondary payload of the Artemis-1 mission. Following deployment near Earth, LIC will employ its low-thrust engine to transfer to a highly inclined 100-km by 5000-km lunar orbit. Designing a trajectory from deployment to the science orbit is made challenging by the large change in energy required and the limited control authority of LIC. To address these challenges, a framework is proposed that leverages dynamical structures available in the bicircular restricted four-body problem (BCR4BP) and direct collocation to design the LIC transfer trajectory. Utilizing the BCR4BP enables the perturbing acceleration of the Sun to assist in the required energy change and avoids the additional complexities of an ephemeris model. Furthermore, direct collocation is a robust technique that permits a greater number of initial guesses to be converged to continuous low-thrust transfers. This framework is demonstrated for multiple launch dates and a subset of results are transitioned to a full ephemeris model for validation. The flexibility and robustness of this framework make it well suited for LIC and other small satellites destined for the Moon that must adapt their trajectory to the needs of a primary payload.

INTRODUCTION

The number of CubeSats launched per year has increased considerably in the last decade with no signs of slowing. This trend is motivated by the low cost and low risk of CubeSat missions compared to their larger counterparts and is enabled by advancements in spacecraft technology miniaturization along with a greater availability of launch opportunities. The vast majority of CubeSat missions thus far have remained in low-Earth orbit (LEO); however, an increasing number of missions are pursuing applications in regions well beyond LEO. The two MarCO spacecraft became the first interplanetary CubeSats when they were deployed from the cruise stage of the *Insight* lander and flew by Mars in 2018.[1] In the near future, thirteen CubeSats will launch as secondary payloads aboard the Artemis-1 mission which delivers an uncrewed *Orion* spacecraft on a test flight around the Moon. All of these CubeSats are bound for destinations beyond LEO. Some, such as the Near Earth Asteroid Scout (NEA Scout) and the CubeSat for Solar Particles (CuSP), will reach heliocentric space. Others, for example Lunar IceCube, Lunar Flashlight, and LunaH-Map, expect to enter orbits about the Moon. The CubeSats aboard Artemis-1 will further demonstrate the utility of the CubeSat platform in more far-flung regions of space and motivate the development of similar missions. Already a new set of CubeSat missions are being developed as secondary payloads for the Artemis-2 mission.

[*]Ph.D. Candidate, School of Aeronautics and Astronautics, Purdue University, West Lafayette, IN, 47907; pritcher@purdue.edu.

[†]Hsu Lo Distinguished Professor of Aeronautics and Astronautics, School of Aeronautics and Astronautics, Purdue University, West Lafayette, IN, 47907; howell@purdue.edu

[‡]Senior Fellow, NASA Goddard Space Flight Center, affiliation, Greenbelt, MD, 20771; david.c.folta@nasa.gov

While the CubeSat revolution brings extraordinary new opportunities for conducting science and demonstrating new technologies, it also introduces new challenges for engineers. Despite technological improvements, ambitious CubeSat missions often involve learning to do "more with less". Some mission design scenarios are enabled via innovative trajectory design approaches that fully exploit natural dynamics. The Lunar IceCube (LIC) concept offers an excellent example of the challenges. This mission will deliver a 6U CubeSat to a low lunar orbit (LLO) where LIC will collect data on water transport throughout the lunar surface. A challenging trajectory design scenario emerges, as the vast change in energy required to transfer from the initial deployment state to LLO is compounded by the limited control authority of the LIC low-thrust engine. Furthermore, as a secondary payload, LIC is subject to changes in the launch date and the conditions required by the primary mission. These challenges necessitate a trajectory design strategy that is flexible and incorporates natural forces to assist with the required energy change.

This investigation extends the trajectory design framework first described by Pritchett, Howell, and Folta[2] by demonstrating its applicability to multiple launch dates and validating sections of the resulting trajectories in an ephemeris model. The proposed framework addresses the challenges of the Lunar IceCube mission by utilizing dynamical structures available in the Bicircular Restricted Four-Body Problem (BCR4BP) along with a robust direct collocation algorithm. Designing in the BCR4BP enables the gravitational force of the Sun to be leveraged to achieve part of the required energy change, while avoiding the additional perturbations of a full ephemeris model. A key feature of the proposed design approach is the use of a staging orbit near the Moon to split the trajectory into two phases: the first from spacecraft deployment to the staging orbit, and the second from the staging orbit to the science orbit. This choice allows the two halves of the LIC trajectory to be designed mostly independently, thus, simplifying the redesign process if deployment conditions change. Moreover, a periodic orbit in the BCR4BP is employed as the staging orbit to leverage its invariant manifolds for the design of efficient paths to and from the staging orbit. Another crucial component of the proposed framework is a direct collocation algorithm to correct initial guesses developed in the BCR4BP into optimal low-thrust trajectories. The robust convergence properties of direct collocation facilitate a wider variety of initial guesses despite large discontinuities in states or time. Together, these key design choices produce a design process that directly addresses the challenges of the Lunar IceCube mission. After an overview of the necessary background, the proposed trajectory design framework is described. Sample Lunar IceCube trajectories are constructed in the BCR4BP for three different deployment dates using the proposed strategies. Additionally, a portion of these trajectories are validated in an ephemeris model. While the trajectory design procedure is applied to the Lunar IceCube mission, it is sufficiently general for a wide variety of low-thrust missions especially those with limited control authority.

BACKGROUND

Previous Work

First proposed in 2015, the Lunar IceCube (LIC) mission is a collaborative effort led by Morehead State University and supported by Goddard Space Flight Center (GSFC), the Jet Propulsion Laborartory, and Busek.[3] The primary objective of this mission is to study the presence and movement of water in all its forms across a broad swath of the lunar surface. To enable the science collection, the 6U CubeSat conducts science operations in a low lunar orbit (LLO) that covers a range of longitudes on the sunlit side of the Moon with a perilune altitude of 100 km. The full set of Keplerian orbital elements that define the science orbit are summarized in Table 1 and are driven by

the science requirements as well as the desire to maximize spacecraft lifetime while minimizing the station-keeping cost.[4] Station-keeping and the transfer trajectory to the science orbit are achieved

Table 1. Lunar IceCube science orbit Keplerian orbital elements defined in a Moon-centered inertial frame. Inclination is measured relative to the Moon's equator and the right ascension of the ascending node (RAAN) is defined with respect to the vernal equinox vector.

Orbital Element	Value
Semi-Major Axis, a	4271.4 km
Eccenctricity, e	0.5697
Inclination, i	$89.35°$
RAAN, Ω	$65°$
Argument of Periapsis, ω	$355°$

via a BIT-3 Busek ion thruster, which is capable of a maximum thrust of 1.24 mN, a specific impulse (I_{sp}) of 2640 seconds, and storing up to 1.5 kg of propellant.[5] Given the total 14 kg mass of LIC, these engine characteristics equip it with a maximum acceleration of 8.857×10^{-5} m/s^2. This value is comparable to the maximum acceleration values for other recent low-thrust spacecraft including Dawn.[6]

The primary mission design challenge for LIC is that its low-thrust engine must deliver a massive change in energy to transfer from the high-energy deployment state near the Earth to the low-energy LLO. While the initial velocity of LIC relative to the Earth is less than escape velocity, the subsequent ballistic path includes a flyby of the Moon that allows LIC to escape the Earth-Moon system. Low-thrust maneuvers are initiated shortly after deployment to prevent escape. In contrast to this high-energy deployment, the LIC science orbit possesses an energy sufficiently low to ensure that the spacecraft is securely captured at the Moon. Despite the challenge of achieving this large change in energy, engineers at GSFC have developed baseline trajectories for a range of potential deployment dates. The most recent launch date provided for Lunar IceCube is November 6^{th} 2020. Each time a new deployment state and epoch are provided, the baseline trajectory must be redesigned. Experience has demonstrated that varying the launch date can significantly impact the geometry of trajectories that deliver LIC to the science orbit.

Faced with a challenging trajectory design scenario and uncertain launch conditions, engineers at GSFC have been informed by the results of several investigations on LIC trajectory design. A strategy that utilizes the high-fidelity General Mission Analysis Tool (GMAT) to design an LIC trajectory with a capture orbit at the Moon is offered by Mathur.[7] An innovative design approach for LIC is also presented by Bosanac, Folta, Cox, and Howell; the Lunar IceCube trajectory is subdivided into three phases: deployment, phasing and energy adjustment, and lunar capture. A strategy for linking these phases that incorporates periapse maps and phasing arcs generated in the Sun-Earth Circular Restricted Three-Body Problem (CR3BP) or the BCR4BP is developed by Bosanac et al.[8–10] Particular focus on the dynamics of the lunar capture phase is delivered separately by Folta et al.[11] The strategy by Bosanac et al. is effective, and recent investigation by Pritchett, Howell, and Folta expanded upon this work by approaching the design problem with a framework that utilizes BCR4BP dynamical structures and direct collocation.[2] The current analysis extends this recent strategy by demonstrating application of the proposed framework to multiple deployment dates and validating some results in an ephemeris model. A comprehensive review of the literature that supports the present work is available in the previous paper by Pritchett, Howell, and Folta.[2]

Bicircular Restricted Four-Body Problem

The BCR4BP builds on the assumptions of the CR3BP. The CR3BP models the path of a third body, P_3, under the influence of two more massive primary bodies, P_1 and P_2. These bodies are assumed to follow circular Keplerian orbits about their mutual barycenter, B_1. Additionally, the third body is assumed to possess negligible mass in comparison to the primary bodies, and this assumption is reasonable when the mass of the third body is quite small, e.g., a spacecraft. Finally, the mass ratio of P_1 and P_2 is denoted, $\mu = \frac{m_2}{m_1+m_2}$, and characterizes the CR3BP system.

The BCR4BP assumes the addition of a fourth body, P_4; both P_4 and the P_1-P_2 barycenter, B_1, move on circular orbits about their mutual barycenter, B_2. In this investigation, P_4 is always the Sun, thus the mass of P_4 equals the mass of the Sun, m_S. The circular orbits of P_1 and P_2 are not affected by the gravitational force of the Sun. As a result of this assumption, the BCR4BP is *not coherent* because the motion of P_1 and P_2 are not influenced by the Sun, i.e., the indirect effects of the Sun are not incorporated. Additionally, as in the CR3BP, the mass of P_3 is assumed to be negligible relative to the other three bodies, i.e., $m_3 \ll m_2 < m_1 < m_S$. In general, the BCR4BP does not require that the Sun-B_1 orbit be coplanar with the P_1-P_2 orbit; however, in this investigation a coplanar model is employed. This model as well as a non-coplanar formulation are presented by Boudad.[12]

It is insightful to examine motion in the BCR4BP from the perspective of two different rotating reference frames. The first is a reference frame rotating with P_1 and P_2, whose axes are defined by three orthogonal unit vectors. By convention, the $\hat{x}$ unit vector of this frame points from P_1 to P_2, while the $\hat{z}$ unit vector is parallel to the angular momentum vector of P_2 about P_1. Finally, the $\hat{y}$ unit vector is defined to complete the orthonormal set. A similar second rotating reference frame is defined for the Sun and B_1, but the $\hat{x}'$ unit vector is instead directed towards B_1 from the Sun. Quantities expressed in the Sun-B_1 rotating frame are generally denoted with a prime, e.g., x' is the x position coordinate of P_3 in the Sun-B_1 rotating frame. Incorporating the coplanar assumption, the orbit of the Sun as viewed from the P_1-P_2 rotating frame is modeled as illustrated in Figure 1. The position of the Sun in the P_1-P_2 rotating frame is determined by the Sun angle, θ_S, and the

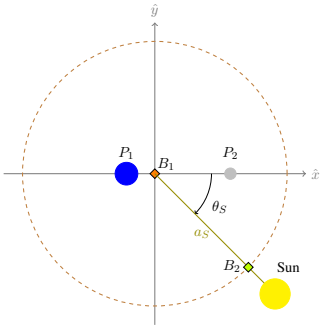

Figure 1. Definition of the Sun angle in the Bicircular Restricted Four-Body Problem.

distance from B_1 to the Sun is defined by the constant value a_S. Viewed from this frame, the Sun rotates clockwise about B_1, thus, the value of θ_S decreases with time.

Motion in the BCR4BP is described by a set of differential equations similar to those in the CR3BP, but modified to accommodate the perturbing acceleration of the Sun. The P_1-P_2 rotating frame together with the Sun-B_1 rotating frame are commonly employed for analysis in the BCR4BP,

and the equations of motion for P_3 may be expressed in either of these frames. The differential equations governing the motion of P_3, expressed in the P_1-P_2 frame and including a low-thrust force, are,

$$\ddot{x} = 2\dot{y} + \frac{\partial \Psi}{\partial x} + \frac{T_x}{m} \qquad \ddot{y} = -2\dot{x} + \frac{\partial \Psi}{\partial y} + \frac{T_y}{m} \qquad \ddot{z} = \frac{\partial \Psi}{\partial z} + \frac{T_z}{m} \qquad \dot{m} = \frac{T}{v_e} \tag{1}$$

where the low-thrust force is represented by the three components of the thrust vector T_x, T_y, and T_z. The magnitude of the thrust vector, $||\boldsymbol{T}|| = T$, appears in the $\dot{m}$ equation, along with the exhaust velocity, v_e. Together these parameters define the mass flow rate of the spacecraft, $\dot{m}$. Additionally, Ψ is the system pseudo-potential written in terms of P_1-P_2 rotating frames coordinates. This pseudo-potential is expressed as,

$$\Psi = \frac{1-\mu}{r_{13}} + \frac{\mu}{r_{23}} + \frac{1}{2}(x^2 + y^2) + \frac{m_S}{r_{S3}} - \frac{m_S}{a_S^3}\left(x_S x + y_S y + z_S z\right) \tag{2}$$

where the distance from the Sun to P_3 is represented by r_{S3}. Together Equations 1 and 2 govern motion in the BCR4BP.

To facilitate numerical computation, the dependent variables in this dynamical model are nondimensionalized via a set of characteristic quantities. The values of the characteristic quantities are determined by the frame in which the states are expressed. When states are expressed in the P_1-P_2 rotating frame, the characteristic length, l^*, is defined as the distance between P_1 and P_2; the characteristic mass, m^*, is equal to the combined mass of P_1 and P_2; and the characteristic time is determined such that the nondimensional angular velocity of P_1 and P_2 is equal to one. The characteristic quantities are defined similarly when states are expressed in the Sun-B_1 rotating frame, except that the parameters of the Sun and B_1 replace those of P_1 and P_2 from the previous case. In this investigation, numerical propagation incorporates the equations of motion expressed in the P_1-P_2 rotating frame. When a low-thrust force is included in the BCR4BP equations of motion the value of m^* is set to the initial mass of the spacecraft.

In contrast to the CR3BP, the BCR4BP is not an autonomous system, i.e., motion in this model is time dependent. As a consequence, this system possesses no integral of the motion. However, the Hamiltonian serves as a useful metric for analyzing the motion of P_3 in the BCR4BP. The Hamiltonian defined in this investigation does not include the low-thrust force, thus, it represents only the ballistic energy of the system. The Hamiltonian may be computed using coordinates expressed in either the P_1-P_2 or Sun-B_1 rotating frames, here it is formulated with coordinates expressed in the former frame,

$$H = 2\Psi - (\dot{x}^2 + \dot{y}^2 + \dot{z}^2) - \sigma \tag{3}$$

The scalar value of H is scaled by a constant parameter σ that is incorporated to offset the high value terms introduced by the Sun and ensure that H is of a similar magnitude to the Jacobi constant value in the Earth-Moon CR3BP. Throughout this analysis, $\sigma = 1690$ nondimensional units.

The same types of dynamical structures that are available in the CR3BP also emerge in the BCR4BP, namely, periodic and quasi-periodic orbits as well as their invariant manifolds. Because the BCR4BP is non-autonomous, these structures are not only defined by position and velocity states, but also by specific epochs, i.e., Sun angles. A periodic orbit in the BCR4BP requires a repetition of the same position and velocity states at the same Sun angle. This angle requirement implies that all periodic orbits in the Sun-Earth-Moon BCR4BP possess a resonance with the synodic period

of the Sun, approximately 29.5 days. The Sun angle, θ_S, completes a full revolution once every synodic period. For example, a periodic halo orbit in the Sun-Earth-Moon BCR4BP, that is computed about the Earth-Moon L_2 libration point, is displayed in Figure 2(a). This orbit possesses a 2:1

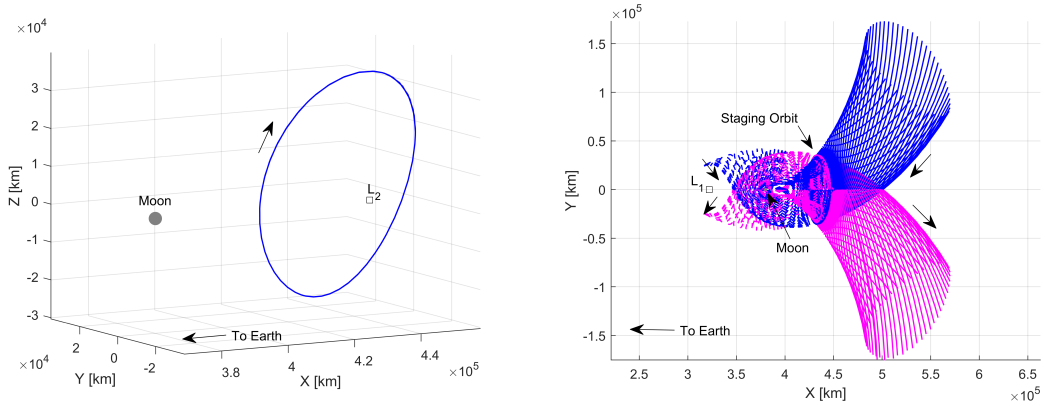

(a) Deployment Trajectories

(b) Staging Orbit Invariant Manifolds

Figure 2. (a) 2:1 synodic resonance halo orbit in the Sun-Earth-Moon BCR4BP that is computed about the Earth-Moon L_2 libration point. This orbit is used as a staging orbit in the proposed design framework. (b) Stable (blue) and unstable (magenta) manifold trajectories plotted in the Earth-Moon rotating frame and originating from the 2:1 resonant L_2 halo orbit displayed in Figure 2(a).

synodic resonance, i.e., two revolutions along the halo orbit are completed for every one synodic period. Similarly, the individual trajectories along the invariant manifold associated with a periodic orbit in the BCR4BP are associated with unique Sun angles. Every path along a stable or unstable manifold arrives at or departs from the periodic orbit at a specific Sun angle. Structures available in the BCR4BP can appear similar to those in the CR3BP, but the dependency on Sun angle is critical.

N-Body Ephemeris Model

While it is frequently convenient to complete preliminary mission analysis in a simplified dynamical model, all trajectory designs must be validated in a higher-fidelity dynamical model. An N-body ephemeris model is frequently employed for this validation step. This model uses the N-body equations of motion to compute the path of a particle, m_i, whose mass is assumed negligible relative to the $N-1$ other bodies included in the model. The motion of the particle of interest is typically expressed in an inertial reference frame that is fixed at one of the massive bodies, denoted the central body, m_q. The $N-2$ other bodies included in the model are considered perturbing bodies, m_p, and these exert additional accelerations on the particle of interest. All massive bodies included in this model are assumed to be centrobaric point masses, and their paths relative to the central body are defined at each instant in time with ephemeris data. The system of equations that results from this formulation governs the path of the particle of interest, that is,

$$\ddot{\boldsymbol{p}}_{qi} = -G\frac{m_i + m_q}{p_{qi}^3}\boldsymbol{p}_{qi} + G\sum_{\substack{j=1 \\ j\neq i,q}} m_j \left(\frac{\boldsymbol{p}_{ij}}{p_{ij}^3} - \frac{\boldsymbol{p}_{qj}}{p_{qj}^3}\right) \tag{4}$$

where G is the universal gravitational constant, $\boldsymbol{p}_{qi}$ is the position vector from the central body to the particle of interest, and p_{qi} is the magnitude of this vector. Similarly, $\boldsymbol{p}_{ij}$ and $\boldsymbol{p}_{qj}$ are position

vectors to the perturbing bodies from the particle of interest and the central body, respectively. In this investigation, the ephemeris data employed to define $\boldsymbol{p}_{qj}$ is obtained from the DE438 ephemerides file, issued by the Jet Propulsion Laboratory Navigation and Ancillary Information Facility. Because the applications in this investigation focus on trajectories in the Earth-Moon system, one of these two bodies is typically employed as the central body while the other body, along with the Sun, are included as additional perturbing bodies. The initial epoch values used for ephemeris model simulations are offered in the text.

Direct Collocation

The process of discretizing a continuous optimal control problem to allow a numerical solution is denoted transcription, and collocation offers one approach to this procedure. A collocation scheme uses polynomials to approximate a solution to the set of differential equations that govern a dynamical model, for example, Equation (1). A collocation problem is discretized into n segments where the dynamics along each segment are approximated by a polynomial. Many collocation schemes are differentiated by the type and degree of the polynomial; this investigation employs 7^{th} degree Legendre Gauss polynomials. Collocation is the transcription method of choice in this investigation due to its wide basin of convergence and amenability to the addition of constraints. Collocation often exhibits a wider basin of convergence than other approaches for solving a system of differential equations, i.e., it will converge upon a solution despite a poor initial guess, even when other methods fail. Since this investigation utilizes direct optimization, the overall optimization approach employed here is termed *direct collocation*.

The tool that implements direct collocation for this investigation is labelled COLT (Collocation with Optimization for Low-Thrust) and was developed in collaboration with Daniel Grebow at the Jet Propulsion Laboratory. The direct collocation framework in COLT generally follows the scheme developed by Grebow and Pavlak and implemented in their MColl software.[13] This scheme is demonstrated to successfully solve many types of of low-thrust trajectory design problems.[2,14–16] Greater detail on the implementation of COLT is available in these previous works.

Nearest Neighbor Search

The proposed trajectory design framework employs maps to aid the construction of initial guesses that are passed to the direct collocation algorithm. Maps capture the returns of trajectory segments to a particular hyperplane, Σ. Frequently, maps are used to facilitate the identification of close connections between two sections of a spacecraft trajectory, e.g., one propagated forward in time and the other backward. Points along these trajectories that intersect the selected hyperplane are displayed on the map. Example hyperplanes include a plane in configuration space, e.g., the xy-plane, or the occurrence of a specific epoch. In this investigation the Sun angle, θ_S, is used to define hyperplanes for two different maps. Parameters such as position, velocity, or energy at the hyperplane intersections may be displayed on the map. The maps in this analysis include points, i.e., hyperplane crossings, from many trajectories, and each trajectory can possess multiple returns to the hyperplane. Due to the large number of points and multiple dimensions of each point plotted on the map it can be challenging to visually identify the best connections between trajectory segments. Therefore, a nearest neighbor search algorithm aids the identification of points on maps that share similar characteristics.

Nearest neighbor (NN) algorithms are employed in many computer science fields under a variety of names.[17] Fundamentally, the nearest neighbor problem involves locating the point p in a set

of points P with the shortest distance to a given point q, assuming all points occupy a space of dimension d.[18] In the present application, hyperplane intersections of the forward propagated group of trajectories provide one set of points, while intersections of the backward propagated trajectories comprise the other set. Thus, an NN search is ideally suited for identifying close connections between these two sets. The tool *Poincare*, developed at JPL, employs NN algorithms for this purpose.[19] In this investigation, Matlab's `knnsearch` algorithm is employed for the NN search. Furthermore, a standardized Euclidean distance metric is used to compute the distances between points. Eight parameters associated with each hyperplane intersection are utilized as NN search criteria in this investigation: the six position and velocity states, the value of the Hamiltonian, H, and the angle of the xy-plane projection of the velocity vector with respect to $\hat{x}$. While the Hamiltonian and in-plane velocity vector angle do not include any information not provided by the states their inclusion has been observed to improve the quality of the matches identified by the NN search algorithm. Because these eight parameters can possess different magnitudes, the standardized Euclidean distance metric applies scaling to prevent one set of parameters from biasing the search. The standard deviations of each of the NN search parameters are used as scaling factors. If desired, the scaling factors may be weighted to emphasize close matches in specific parameters. This weighting is achieved by decreasing the value of the scaling factors for the parameters that are to be emphasized. The NN search algorithm is a useful tool that complements visual inspection of maps to identify close connections between trajectory segments.

TRAJECTORY DESIGN FRAMEWORK

The proposed trajectory design framework is distinguished by three key features: modeling in the BCR4BP, employing a staging orbit, and computing low-thrust transfers with direct collocation. Together, these design choices deliver a flexible and robust procedure for constructing the LIC trajectory. A staging orbit near the Moon is used to divide the mission design challenge into two phases, as illustrated in Figure 3. Phase 1 occurs from deployment to the staging orbit and Phase

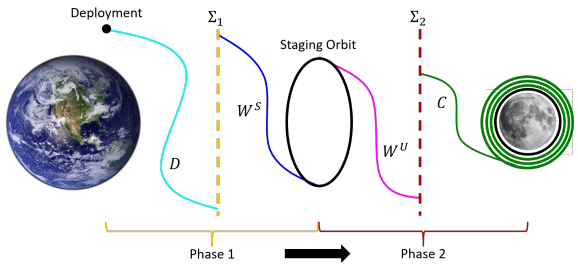

Figure 3. Schematic of trajectory design framework.

2 passes from the staging orbit to the low lunar altitude science orbit. Use of the staging orbit facilitates the division of the end-to-end Lunar IceCube trajectory into these two distinct phases, thus, mitigating some of the design challenge. Initial guesses for each phase are generated nearly independently of one another. Discrepancies in epoch between the two phases that result from this independence can be overcome by waiting in the staging orbit until the desired departure epoch is reached. Initial guesses for both phases of the trajectory design framework are assembled with the aid of two different maps. These maps display intersections with the hyperplanes Σ_1 and Σ_2 which are defined by the Sun angles θ_{S_1} and θ_{S_2}, respectively. The first map captures intersections of Σ_1 by forward propagated deployment trajectory arcs, D, and backward propagated paths on the

stable manifold of the staging orbit, W^S. Similarly, the second map captures intersections of Σ_2 by forward propagated trajectories on the unstable manifold of the staging orbit, W^U, and backward propagated capture trajectory arcs, C. Close matches between hyperplane intersections of forward and backward propagated trajectories are identified and their corresponding trajectory segments are assembled into an initial guess for the direct collocation tool COLT.

Phase 1: Deployment to Staging Orbit

Design of Phase 1 of the LIC trajectory is facilitated by the creation of maps that display intersections of Σ_1 along trajectories propagated forward from deployment and backward on the stable invariant manifold of the staging orbit. To expand the options available on these maps, a range of D and W^S trajectory arcs are generated. Different W^S arcs are obtained by changing the state and epoch of the departure point from the periodic orbit. In contrast, because the deployment state and epoch cannot be changed, a span of D trajectory segments is generated by varying thrust direction prior to the first Lunar flyby. Three different deployment dates are considered in this investigation; these dates, and their corresponding initial Sun angles are displayed in Table 2.

Table 2. Deployment dates and corresponding Sun angles considered for Lunar IceCube. The final date is the current launch date of Lunar IceCube.

Deployment Date	Initial Sun Angle [rad]
Oct. 9$^{\text{th}}$, 2018	6.1557
Jun. 27$^{\text{th}}$, 2020	4.8193
Nov. 6$^{\text{th}}$, 2020	2.0185

Trajectories propagated forward in time from the deployment condition, D, are divided into three parts, an initial coast period, a thrust segment, and a second coast period. An example of this subdivision is displayed in Figure 4(a). The duration of the first coast segment is set to 0.8 days. While this time can be modified, a minimum 8 hour initial coast period must be allowed for performing spacecraft systems checkouts and obtaining tracking data. Following this coasting period, a multi-day thrust segment is introduced. A thrust segment of three days is used in this investigation; however, this value can be altered to change the post-flyby behavior of the deployment trajectory. The direction of the thrust vector along this segment is varied to generate a range of deployment trajectories. The angle, α, used to determine the thrust vector direction is defined relative to the $\hat{v}$ unit vector in the velocity-normal-binormal (VNB) frame. This frame is defined such that the $\hat{v}$ unit vector is in the direction of the velocity vector of the spacecraft expressed in the rotating frame. Additionally, the $\hat{n}$ unit vector is in the direction of the spacecraft's angular momentum vector relative to B_1, and the $\hat{b}$ unit vector is defined to complete the orthonormal set. The angle α determines the direction of the thrust vector in the vb-plane, and no out-of-plane, i.e., $\hat{n}$ component of the thrust vector, is introduced. By varying α from 0° to 360° many different post-flyby trajectories are generated, as seen in Figure 4(a). Following the thrust segment, a second coast segment is propagated for a user-defined number of days. Intersections of this second set of coast arcs, labeled D in Figure 3, with the hyperplane Σ_1 are recorded and used to generate the map. Any D trajectory arcs that impact the Moon are excluded from the map.

The forward propagated D trajectory arcs are linked to trajectories propagated backward in time along the stable manifold, W^S, of the staging orbit. The stable invariant manifolds of periodic orbits

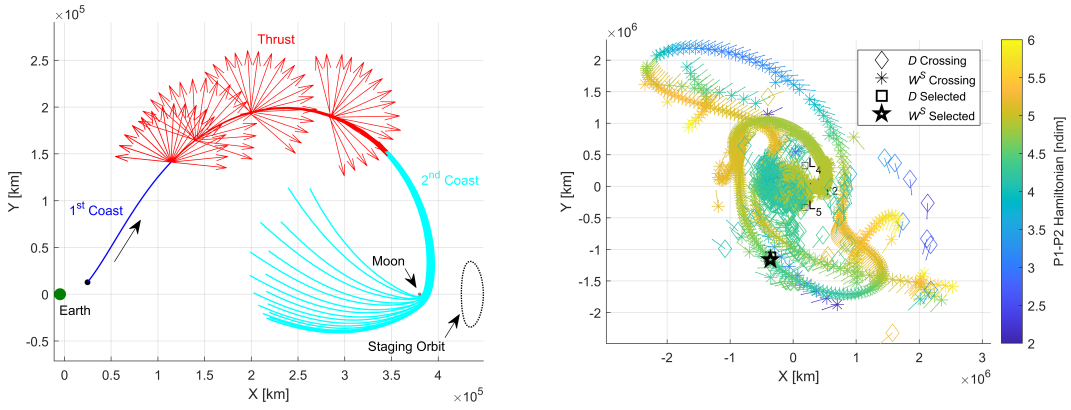

(a) Deployment Trajectories

(b) Phase 1 Map in E-M Rotating Frame

Figure 4. (a) Sample range for deployment trajectories in the creation of a Phase 1 map, plotted in the Earth-Moon rotating frame. The first coast period is 0.8 days, the thrust segment is 3 days, and the second coast section is 4 days. Thrust vectors span a range of α angle values from 0 to 360° in the VNB frame. Trajectories that impact the Moon are omitted. (b) Map of Σ_1 intersections of the forward propagated D and backward propagated W^S trajectory arcs in the BCR4BP. Intersections are projected in the xy-plane of the Earth-Moon rotating frame. This map is generated for the June 2020 deployment and using a Σ_1 Sun angle of $\theta_{S_1} = 318^\circ$.

offer efficient paths onto the orbits. Thus, using these trajectories to guide LIC to the staging orbit should lead to a solution that requires less propellant than other potential insertion paths. Figure 2(b) displays trajectories along the stable manifold. The initial trend of these manifold paths is either in the positive or negative x direction. In the former case, trajectories on the manifold tend to escape the Earth-Moon system, and these paths offer more useful connection points with the D trajectory arcs. Stepping off the periodic orbit and onto the stable manifold at different states and epochs around the orbit generates the range of manifold paths observed in Figure 2(b).

A map is created to join the two halves of the Phase 1 LIC trajectory by recording intersections of the D and W^S trajectory arcs with Σ_1. Trajectories are propagated until either a maximum time limit or a maximum distance from the Earth is reached. In this case, a maximum time of 100 days and a maximum Earth distance of 3×10^6 km are used for both the D and W^S propagation. An example map is displayed in Figure 4(b) where the Sun angle at which events are recorded is $\theta_{S_1} = 318^\circ$. The events that occur along the D trajectories are plotted as diamonds, while the events on the W^S arcs are marked as asterisks. All events are plotted in the Earth-Moon rotating frame, and each marker is colored according to the Hamiltonian, H, of the spacecraft at the time of the event. Additionally, the spacecraft's xy-plane velocity direction is plotted as an arrow centered at the marker. Adding this extra information to each plot aids the identification of close matches between D and W^S trajectories. A balance of small discontinuities in position as well as velocity magnitude and direction is desired. However, despite the added map features the large number of points on each map make it challenging to visually identify promising intersections. To alleviate this difficulty an NN algorithm is employed to identify the top matches between intersections on a map. Furthermore, because the NN algorithm significantly decreases the time required to identify useful matches on a single map, this tool is leveraged to rapidly search many maps across a range of θ_{S_1}. This capability further improves the quality of the identified matches and therefore the utility

of the corresponding initial guesses generated for Phase 1. A close match, identified by the nearest neighbor algorithm, is highlighted in Figure 4(b). The D and W^S trajectories are propagated to the selected intersection times and used as an initial guess for the direct collocation algorithm in the Sample Trajectory Design section.

Phase 2: Staging Orbit to Science Orbit

Phase 2 of the LIC trajectory consists of the transfer from the staging orbit to the science orbit. An initial guess for this phase is assembled in a similar manner to Phase 1; intersections with Σ_2, along a range of forward and backward propagated trajectories, are plotted on a map used to select the initial guess. In this case, paths along the unstable manifold, W^U, of the staging orbit make up the forward propagated trajectory segments. The backward propagated segments, C, consist of trajectories propagated with low-thrust, in reverse time, from different true anomaly values on the science orbit. The map used to link the forward and backward propagated trajectories consists of intersections with Σ_2, defined by the Sun angle θ_{S_2}, along these trajectory segments.

Trajectories along the unstable manifold, W^U of the staging orbit offer energy efficient paths for departing the orbit and beginning the spiral down to the science orbit. Apart from their inverse direction, these trajectories behave similarly to those on the stable manifold and are displayed in Figure 2(b). Paths on W^U offer a variety of locations and epochs at which to depart the staging orbit, and intersections with Σ_2 along these trajectories populate the Phase 2 map.

To generate a range of C trajectories that insert onto the final orbit, backward propagation is initiated from true anomaly values on the orbit that span the full 360° range. The backward propagation assumes a maximum thrust anti-velocity control law - that is, the thrust vector is always oriented along the $-\hat{v}$ direction of the VNB frame and has a magnitude equal to the maximum thrust of LIC. Recall that the VNB frame is defined relative to the rotating frame velocity vector. Application of this control law produces a trajectory that, in forward time, gradually spirals down to the final science orbit. While these two quantities are constant for all backward propagated trajectories, using a range of true anomaly values to initialize propagation ensures that each trajectory evolves differently. Trajectories are propagated until either a maximum time limit or a maximum distance from the Earth is reached. In this case, W^U arcs are propagated for a maximum time of 100 days while C trajectory segments are propagated up to 200 days. Both types of trajectories are propagated to a maximum distance from the Earth of 6×10^5 km. Intersections with Σ_2 along each propagated trajectory are recorded and added to the Phase 2 map.

To generate the C trajectory arcs an epoch for insertion onto the science orbit as well as a spacecraft mass at insertion must be assumed. Reasonable inferences for these values made during initial guess formulation are later adjusted by the direct collocation algorithm to ensure a continuous final result. Previous analyses have indicated that the total duration of the LIC transfer is approximately one year, thus this amount is added to the deployment date to obtain an estimated epoch at science orbit insertion (SOI). The SOI epoch is used to compute a corresponding Sun angle, θ_{SOI}, and angle between the inertial and rotating frames, Φ_{SOI}, which are required to propagate the C trajectory arcs in the BCR4BP. Earlier investigations also indicate that LIC consumes approximately half of the available propellant mass to execute the transfer from deployment to science orbit, therefore a final mass at SOI, m_{SOI}, of 13.25 kg is assumed. While this variable can be adjusted in the direct collocation algorithm the initial guess estimate biases the m_{SOI} value of the converged Phase 2 solution. However, this bias is overcome by increasing m_{SOI} via a natural parameter continuation process after an initial solution is converged. Finally, even if an intuition for the epoch and mass at

SOI is not available, the robustness of the direct collocation algorithm increases the likelihood that poor estimates for these values can still produce useful initial guesses.

Intersections with Σ_2 along the W^U and C trajectory segments generated for Phase 2 are projected on the xy-plane and colored according to their H value. These three parameters, along with the in-plane direction of the velocity vector, are used to identify close matches between trajectory segments. An example map is displayed in Figure 5(a) where the Sun angle that defines Σ_2 is $\theta_{S_2} = 66°$. The intersections that occur along the C arcs are plotted as diamonds, while those on

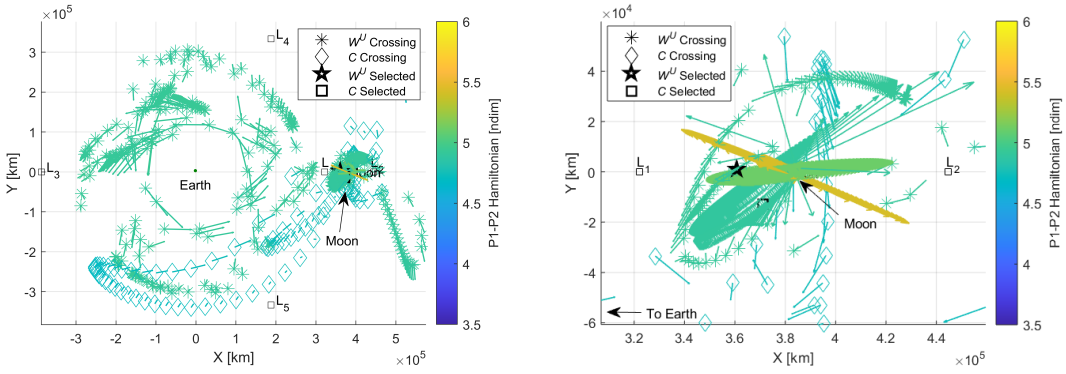

(a) Phase 2 Map in E-M Rotating Frame

(b) Zoomed View of Phase 2 Map Near the Moon

Figure 5. Map of Σ_2 intersections of the forward propagated W^U and backward propagated C trajectory arcs in the BCR4BP. Intersections are projected in the xy-plane of the Earth-Moon rotating frame, and the Sun angle selected for Σ_2 is $\theta_{S_2} = 66°$. The zoomed view displays an intersection selected by the NN search algorithm. This map corresponds to the October 2018 deployment date and assumes an SOI epoch of midnight on September 24^{th}, 2019.

the W^U paths are displayed as asterisks. Once again, a NN algorithm is used to rapidly identify the top matches for maps at a range of θ_{S_2} values. A close match, identified with this process, is highlighted in Figure 5(b). The deployment and manifold trajectories propagated to the selected intersection times are used as an initial guess for the direct collocation algorithm.

Modifications are made to COLT's nominal collocation scheme to enable design of a continuous low-thrust transfer from the staging orbit to the final science orbit for LIC. The low-thrust spiral required to transfer between these two orbits is long and includes many revolutions. This type of trajectory is challenging to optimize using the collocation framework implemented in COLT, which employs Cartesian coordinates. Other collocation schemes that utilize modified equinoctial elements (MEE) have successfully optimized low-thrust spiral trajectories.[20,21] However, rather than implement a complex multi-phase collocation scheme that uses Cartesian and MEE coordinates, a simplified approach is used. This strategy divides Phase 2 into two halves: one is solved with direct collocation and the other is explicitly propagated backward in time from science orbit insertion (SOI).

The backward propagated section of the LIC trajectory is updated in the direct optimization process by the addition of three design variables and a constraint. The three design variables govern: the backward propagation time from SOI, the true anomaly value on the science orbit at insertion, and the spacecraft mass at SOI. By including these variables in the corrections process, the evolu-

tion of the spiraling LIC trajectory is allowed to change and can be joined with the section of the transfer that departs from the staging orbit. A constraint is added to ensure state and mass continuity between these two halves of the LIC trajectory. Experience indicates that convergence is improved when the match point for this constraint is located far away from the Moon. This is due to the increased sensitivity of the constraint partials when the match point is near the Moon. Therefore, initial guesses generated with the Phase 2 map are filtered such that the potential match point is located at least 3 lunar radii from the Moon.

With the addition of the three design variables and constraint, a single direct collocation problem is solved to generate a continuous low-thrust transfer from the staging to the science orbit. Because a sub-optimal control law is used for the spiraling portion of the trajectory, the result of the direct collocation algorithm is not a fully optimized low-thrust transfer. However, optimization is used to minimize the propellant consumed before the explicitly propagated spiraling phase begins. This optimization approach is taken rather than directly optimizing the mass at science orbit insertion, because including this latter variable in the objective function increases the sensitivity of the optimization algorithm to a level that makes achieving converged solutions difficult. A benefit of the selected control law is that it ensures the maximum rate of change of the spacecraft's energy, thus reducing the time required to achieve Lunar capture. By decreasing the time to Lunar capture, the propellant consumption is also reduced. In summary, this approach for computing a trajectory from the staging to the science orbit generates a continuous low-thrust transfer without the complexity of a multi-phase collocation scheme.

SAMPLE TRAJECTORY DESIGN

The proposed trajectory design framework offers a procedure for developing an initial guess for the full Lunar IceCube trajectory, from deployment to insertion on the science orbit. After maps are generated for Phases 1 and 2, close matches between forward and backward propagated trajectory segments are identified with the NN search algorithm. These segments are employed to construct initial guesses for the direct collocation algorithm. This robust algorithm is frequently able to converge even when given very discontinuous initial guesses. Additionally, this methodology may be employed to construct Lunar IceCube transfers with a variety of geometries and which are applicable to a range of deployment dates.

Phase 1: Deployment to Staging Orbit

An initial guess for Phase 1 of the Lunar IceCube trajectory is assembled by using the NN search algorithm to identify close matches between Σ_1 intersections on D and W^S trajectories in a Phase 1 map. The top NN search algorithm results from maps over a range of θ_{S_1} values are examined to identify the most promising candidates and the available transfer geometries. One such match is highlighted by black markers in Figure 4(b), where the black square indicates the deployment event and the black five-pointed star denotes the manifold event. The trajectories that correspond to the selected match are shown in the Sun-B_1 and Earth-Moon rotating frames in Figures 6(a) and 6(b) respectively. These trajectories, and all others that correspond to the map intersections in Figure 4(b), are generated with the November 2020 deployment date. While a discontinuity between the forward and backward propagated trajectories is evident, the NN search criteria used to identify matches between Σ_1 crossings yield a promising initial guess. This initial guess is passed to COLT, which eliminates the discontinuity by inserting additional thrust segments. The optimized trajectory in the BCR4BP that results from this initial guess is displayed in Figure 6(c), and consumes 0.1 kg of

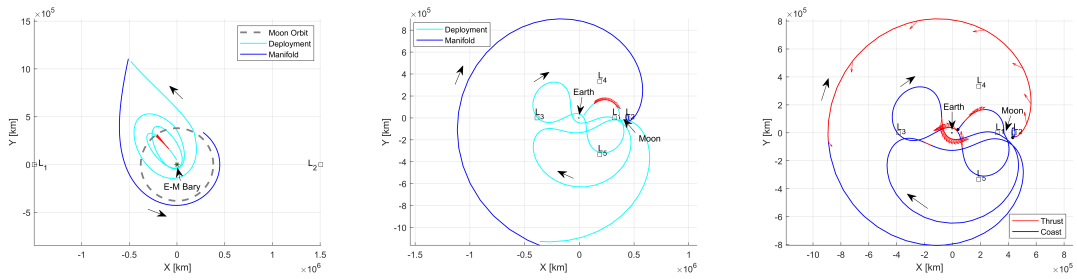

(a) Initial Guess S-B_1 Rot. Frame (b) Initial Guess E-M Rot. Frame (c) Result E-M Rot. Frame

Figure 6. Initial guess and BCR4BP result for Phase 1 of the Lunar IceCube trajectory given a November 2020 deployment date. The resulting transfer requires 117 days and 0.10 kg of propellant. The initial guess is displayed in the Sun-B_1 (S-B_1) and Earth-Moon (E-M) rotating (rot.) frames.

propellant to reach the staging orbit in 117 days. The time of flight (TOF) and mass consumption, Δm, of this and all transfers examined for this investigation are offered in Table 3. An initial 8 hour coast period following deployment is preserved in the converged solution to allow time for systems checkout prior to the beginning of the first thrust arc. The collocation algorithm computes this solution with relatively few iterations; moreover, the geometry of the initial guess is generally preserved in the direct collocation result. These two factors indicate that the initial guess identified with the Phase 1 map was useful in guiding the algorithm towards a solution.

The strong influence of the initial guess on the final result is more evident when alternate solutions are examined. For a single deployment date a range of transfer geometries may be constructed using the Phase 1 maps. These transfers may range from 90 to nearly 200 days in duration and are primarily distinguished by the number of Earth close approaches and lunar flybys they contain. Generally, the longer duration transfers require less propellant due to the inclusion of additional flybys or the opportunity to include thrust arcs at more optimal times, such as Earth close approach. While launch conditions determine some of the available transfer geometries every launch date yields a plethora of options. A Phase 1 transfer generated for the June 2020 launch date, shown in Figure 7, offers an example of an alternate Phase 1 geometry. This transfer possesses no Earth close approaches and instead performs several transits around the Earth-Moon system before delivering the spacecraft to the staging orbit. In total this transfer requires more time and propellant to execute, however it may be favorable because it avoids the complications of performing Earth close approaches. The June 2020 Phase 1 solution is validated in an ephemeris model and the geometry and propellant consumption of the resulting trajectory, displayed in Figure 7(c), remain nearly the same as the BCR4BP solution. This similarity indicates that the BCR4BP result reasonably approximates the ephemeris model for Phase 1 of the Lunar IceCube transfer.

The final deployment condition tested in this investigation occurs in October 2018. In the Earth-Moon rotating frame the initial path of the deployment trajectory appears similar for all three deployment dates. However, examination in the inertial or Sun-B_1 rotating frames reveals that the initial Sun angle for each deployment state is quite different. These differences in epoch along with changes to the deployment state cause the paths to the staging orbit to be different for each deployment date. The October 2018 Phase 1 trajectory includes two Earth close approaches that appear similar to the November 2020 transfer, however this trajectory differs in that it includes a second lunar flyby. This additional lunar flyby helps make this trajectory the shortest in duration of the

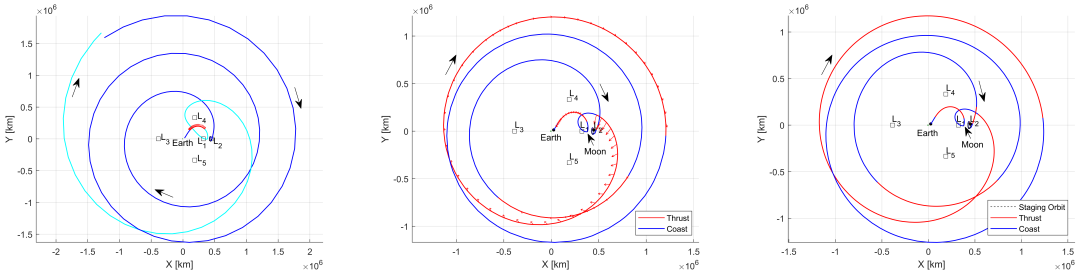

(a) Initial Guess (b) BCR4BP (c) Ephemeris

Figure 7. Initial guess (a) and BCR4BP (b) solutions for Phase 1 of the Lunar IceCube trajectory given a June 2020 deployment date. The resulting BCR4BP transfer requires 140 days and 0.21 kg of propellant. The BCR4BP transfer is validated in an ephemeris model (c) where it maintains similar characteristics.

Phase 1 transfers while only requiring slightly more propellant than the lowest cost transfer. The geometry of this transfer remains consistent when transitioned to an ephemeris model.

Despite the different deployment dates all three Phase 1 transfers take advantage of the tidal forces of the Sun to reach the staging orbit near the Moon. This is evidenced by the fact that the apoapse furthest from the Earth-Moon barycenter, B_1, for of all three transfers occurs in the second quadrant of the Sun-B_1 rotating frame.[12] In this quadrant the acceleration from the Sun is acting in the same direction as the prograde motion of LIC about the Earth-Moon barycenter, B_1. Therefore, the Sun's acceleration tends to circularize LIC's orbit about B_1 helping raise its periapse to the radius of the Moon's orbit.

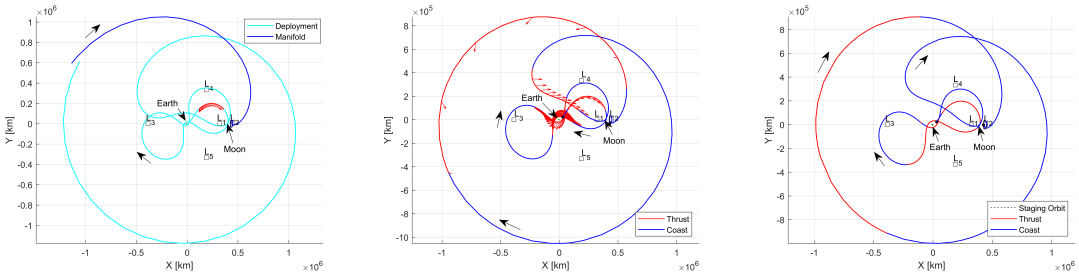

(a) Initial Guess (b) BCR4BP (c) Ephemeris

Figure 8. Initial guess (a) and BCR4BP (b) solution for Phase 1 of the Lunar IceCube trajectory given an October 2018 deployment date. The resulting transfer requires 110 days and 0.1 kg of propellant. The BCR4BP transfer is validated in an ephemeris model (c) where it maintains similar characteristics.

Many different transfer geometries and durations are offered by the NN search results of Phase 1 maps. The examples in Figures 6 through 8 are a small subset of the variety of options available. By experimenting with the top search results from maps generated with a range of θ_{S_1} values, a variety of initial guess geometries can be obtained that lead to an array of optimized solutions. The flexibility of this approach and the diversity of solutions it offers makes it adaptable to different mission constraints and deployment conditions.

Phase 2: Staging Orbit to Science Orbit

A solution for Phase 2 of the LIC trajectory is computed in a similar manner to Phase 1, however some information from the Phase 1 result must be carried over to Phase 2. A close match between Σ_2 crossings on a Phase 2 map is identified and the corresponding trajectory segments are employed as an initial guess for a direct collocation algorithm that computes a continuous solution. While little information from Phase 1 is required to generate the initial guess for Phase 2, the time of flight and final mass of a specific Phase 1 transfer is necessary to actually converge a Phase 2 transfer. This information is used to initialize the spacecraft mass and Φ angle for Phase 2, thus ensuring a continuous transfer between the two phases.

Nearby intersections of W^U and C arcs on a Phase 2 map are located using the NN search algorithm. An example of a close match between Σ_2 crossings on a Phase 2 map is identified in Figure 5(b). Because the staging orbit and the science orbit are significantly out-of-plane, the xy-plane view of the Phase 2 map shown in Figure 5(b) can be deceptive. Hyperplane crossings that appear to overlap in this map may differ significantly when the $\hat{z}$ position and velocity components are considered. Conversely, potentially useful matches may be obscured if intersections with larger $+z$ components are plotted on top of them. For this reason use of the NN search algorithm is even more essential for Phase 2 maps to ensure that close matches are not overlooked.

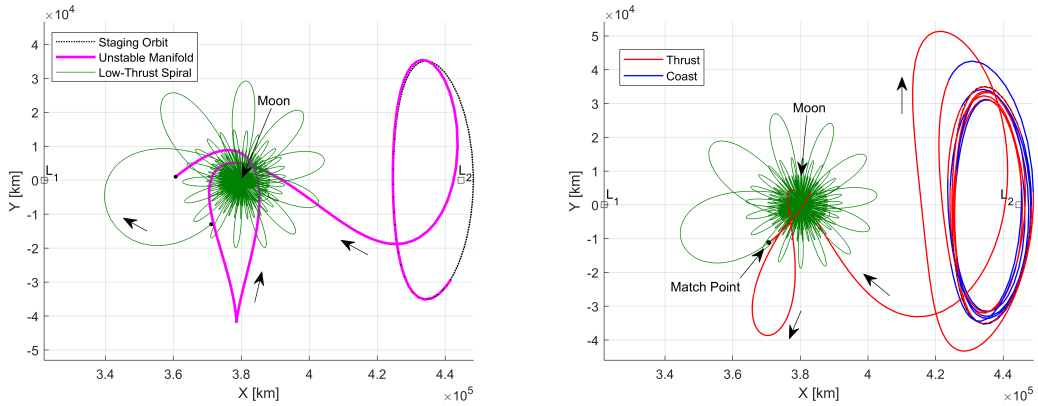

(a) Initial Guess (b) Result

Figure 9. Initial guess and converged result for Phase 2 of the Lunar IceCube trajectory. The endpoints of the unstable manifold and low-thrust spiral trajectory are indicated with a black circle. The Phase 1 result for the October 2018 deployment is used to initialize this transfer. The resulting Phase 2 transfer requires 229 days and 0.5 kg of propellant.

After a promising match is identified the corresponding trajectory segments are employed to construct an initial guess. The trajectories corresponding to the intersections selected in Figure 5(b) are displayed in Figure 9(a). The endpoints of the unstable manifold and low-thrust spiral trajectories are indicated with black circles. Continuity between the departure arc from the staging orbit, solved via collocation, and the explicitly propagated low-thrust spiral is enforced by matching these endpoints, as shown in Figure 9(b). The initial guess is generated such that these endpoints are located at least three lunar radii from the center of the Moon. This is because distance of the match point from the Moon generally increases the likelihood of achieving convergence due to the reduction in sensitivity.

In general, it is more difficult to achieve convergence for Phase 2 of the LIC trajectory. This is because the initial guesses generated by the map possess large state discontinuities near the Moon where strong gravitational forces increase the sensitivity of the direct collocation algorithm. Several additional steps may be taken to increase the likelihood of convergence. These steps include bounding the design variables, scaling variables and constraints, and including a minimum radius constraint with respect to the Moon. Also, convergence may be improved by providing COLT more trajectory, and therefore more time, with which to achieve the desired transfer. This is done by "stacking" additional revolutions of the staging orbit prior to departure on the unstable manifold path.[15] Four additional revolutions on the staging orbit are added to the initial guess displayed in Figure 9(a). Thus, the initial guess passed to COLT consists of these four revolutions, the unstable manifold trajectory, and the backward propagation parameters, i.e., the three additional design variables, that produce the low-thrust spiral displayed in Figure 9(a). Stacking additional staging orbit revolutions is also used to account for discrepancies between the SOI epoch estimated for initial guess design and the actual SOI epoch determined by the Phase 1 transfer selected to initialize the mass and Φ angle of Phase 2. Several iterations of the Phase 2 initial guess design process may be required if the estimated SOI epoch requires too many or too few stacked staging orbit revolutions.

The initial guess displayed in Figure 9(a) is passed to the direct collocation algorithm, COLT, for convergence. From this initial guess COLT computes the low-thrust transfer in Figure 9(b), which requires approximately 229 days and 0.5 kg of propellant to achieve. The solution displayed in Figure 9(b) shows that the stacked staging orbit revolutions included in the initial guess are distributed by the direct collocation algorithm to achieve the changes in energy necessary to deliver the spacecraft to the beginning of the low-thrust spiral. This new motion is more evident in Figure 10(a), a three-dimensional view of the transfer. While these revolutions near the staging orbit

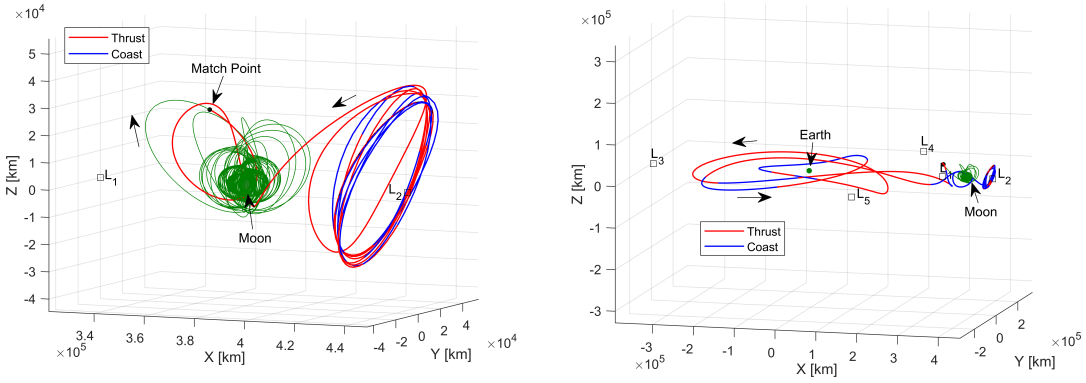

(a) Near Moon (b) Around Earth

Figure 10. Three dimensional views of the two types of transfer geometries available for transiting from the staging orbit to the science orbit. The necessary plane and energy changes required to match the beginning of the low-thrust spiral are executed in different manners in the near Moon versus around Earth geometries.

include a substantial amount of thrusting many of these thrust arcs utilize thrust magnitudes well below the maximum available thrust value. This behavior indicates that it may be possible to reduce the number of staging orbit revolutions stacked in the initial guess for this transfer, thus reducing the transfer time. After several revolutions the spacecraft departs the vicinity of the staging orbit and

conducts a powered lunar flyby to insert on the explicitly propagated low-thrust spiral trajectory. This geometry is influenced by the close lunar flyby included in the initial guess.

Phase 2 transfers generally fall into one of two categories: transfers that remain near the Moon, as seen already, and those that include at least one loop around the Earth. The latter of these two options is observed in a Phase 2 map generated for the November 2020 deployment date. A close connection is identified on a Phase 2 map generated with Σ_2 defined by a Sun angle of $\theta_{S_2} = 75°$, and the resulting initial guess is displayed in Figure 11(a). In this case, the difference in position

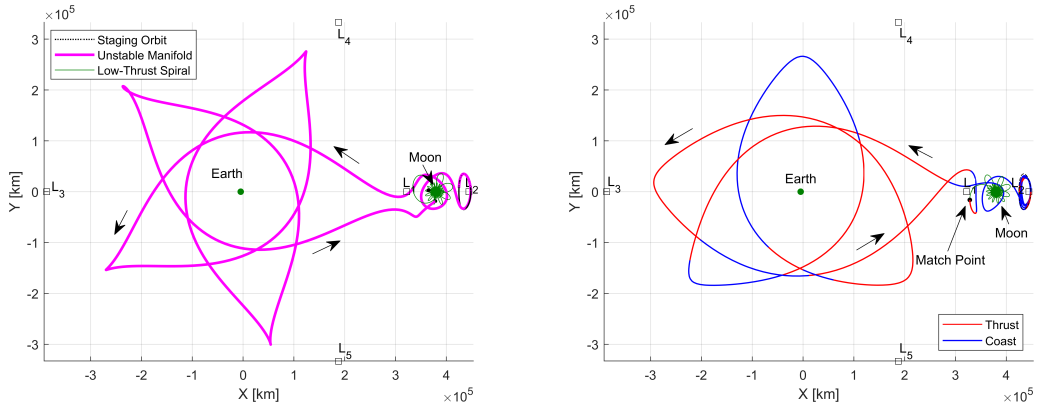

(a) Initial Guess (b) Converged Result

Figure 11. Initial guess and converged result for Phase 2 of the Lunar IceCube trajectory. The Phase 1 result for the November 2020 deployment is used to initialize this transfer. The resulting Phase 2 transfer requires 233 days and 0.65 kg of propellant.

between the end of the unstable manifold trajectory and the beginning of the low-thrust spiral is even larger. However, these two points are relatively close in energy and in velocity direction. Despite the seemingly large discontinuity, COLT uses this initial guess to compute the low-thrust transfer shown in Figure 11(b). This transfer delivers the spacecraft from the staging orbit to the science orbit in 233 days and requires 0.65 kg of propellant mass. Figures 10(b) and 11(b) illustrate that rather than using repeated revolutions near the staging orbit, much of the plane change required to begin the spiral down to the science orbit is completed during the transit around the Earth. This behavior, and the distance of the endpoints from the Moon, make this transfer and others like it easier to converge.

The two basic types of Phase 2 transfer options, near Moon and around Earth geometries, are available regardless of the deployment date. This is because the majority of these transfers occurs well within the Earth-Moon system where the gravitational influences of these two bodies dominate. In this region the influence of the Sun is small enough that it has less effect on the available geometries no matter the value of θ_S. As a consequence, it is possible to design Phase 2 of the transfer in the CR3BP, however this investigation utilizes the BCR4BP in Phase 2 to maintain consistency with Phase 1. Despite the additional complexity the proposed framework is able to successfully design Phase 2 transfers in the BCR4BP for all three deployment dates examined. A summary of the Phase 2 transfers constructed in the BCR4BP for all three deployment dates is available in Table 3. While not displayed here the Phase 2 transfer generated for the June 2020 deployment possesses a near Moon geometry similar to that seen in Figure 9.

Combined Transfer Trajectory Summaries

Combining the results computed for Phases 1 and 2 of the LIC trajectory yields complete deployment to science orbit trajectories. The sample LIC trajectories computed in the BCR4BP using the proposed framework are summarized in Table 3. Note that for all transfer combinations, up to one synodic period of additional transfer time can be added to account for the phasing time that must be included in the staging orbit following Phase 1 of the transfer. This time allows the spacecraft to reach the state and Sun angle required to begin Phase 2. In this investigation, the maximum phasing time required is just over 10 days and the minimum is less than one day. Over two thirds of the total time of flight (TOF) is spent in Phase 2 where the long transfer to the beginning of the low-thrust spiral is followed by a lengthy spiral. Substantial time savings could be achieved by developing methods to reduce the TOF of this phase. In total, all three transfers reach the science orbit about one year after deployment.

Table 3. Summary of sample transfers for all three deployment dates. Given characteristics are time of flight (TOF) [days], change in mass (Δm) [kg], and final mass [kg].

Deployment	Phase 1		Phasing	Phase 2		Total		Final
Date	Δm	TOF	Time	Δm	TOF	Δm	TOF	Mass
Oct. 9^{th}, 2018	0.11	109.82	7.72	0.49	228.87	0.60	346.31	13.40
Jun. 27^{th}, 2020	0.21	139.90	0.89	0.64	229.85	0.85	370.64	13.15
Nov. 6^{th}, 2020	0.10	117.39	10.24	0.55	233.39	0.65	361.02	13.35

The transfer times and propellant consumption values provided in Table 3 are comparable to past baseline trajectories. While some of the transfers computed with the proposed framework require more time and propellant than previous baseline solutions several steps are available that may reduce these parameters. First, some of the staging orbit revolutions added in Phase 2 can be removed. While the additional staging orbit revolutions added to the initial guess are useful to achieve convergence, it may be possible to remove some of them after a transfer is converged. For example, some of the revolutions near the staging orbit that appear in Figure 10(a) could likely be removed because long coast arcs are apparent. If possible, removing excess trajectory will reduce transfer time. Secondly, using a multi-stage collocation algorithm to solve Phase 2 will offer the greatest improvement in delivered mass because the majority of propellant consumption occurs in this phase. A multi-stage approach would permit the low-thrust spiral to the science orbit to be fully optimized, thereby increasing m_{SOI}. These two steps could lead to reductions in both time of flight and propellant consumption for the LIC transfer, and are profitable areas on which to focus future work.

CONCLUDING REMARKS

The proposed framework for constructing an LIC baseline trajectory addresses the need for a design methodology that is both robust and flexible. Employing a dynamical model that includes the Sun enables the perturbing acceleration of this body to be leveraged to achieve the desired transfer despite LIC's limited control authority. Moreover, utilizing direct collocation to converge initial guesses developed in the BCR4BP allows a wider range of guesses to be used due to the robustness of this algorithm. Flexibility is further enhanced by using a staging orbit to separate the LIC trajectory into two halves that can be designed with a degree of independence. Together, these

design choices offer a framework to systematically generate a variety of transfer configurations with time of flight and propellant consumption values comparable to the current baseline. This framework is demonstrated to work for a range of deployment dates and sections of the resulting transfers are verified in an ephemeris model. Suggested further improvements to this procedure could increase the efficiency of the process, enhance the quality of the solutions it generates, and broaden its applicability to missions beyond LIC.

ACKNOWLEDGMENT

The authors thank the Purdue University School of Aeronautics and Astronautics for facilities and support, including access to the Rune and Barbara Eliasen Visualization Laboratory. Additionally, many thanks to the members of the Purdue Multi-Body Dynamics Research Group for interesting discussions and ideas. Special thank you to Nicholas LaFarge for the idea of employing a nearest neighbor search algorithm and for guidance on its implementation. This research is supported by NASA Space Technology Research Fellowship, NASA Grant NNX16AM42H. Some analysis was conducted at the NASA Goddard Space Flight Center.

REFERENCES

[1] J. Schoolcraft, A. T. Klesh, and T. Werne, "MarCO: Interplanetary Mission Development On a CubeSat Scale," *SpaceOps 2016 Conference*, SpaceOps Conferences, American Institute of Aeronautics and Astronautics, May 2016, doi:10.2514/6.2016-2491.

[2] R. E. Pritchett, K. C. Howell, and D. C. Folta, "Low-Thrust Trajectory Design for a Cislunar CubeSat Leveraging Structures from the Bicircular Restricted Four-Body Problem," *70th International Astronautical Congress*, Wasington D.C., 2019, pp. 1–18.

[3] P. Clark, B. Malphrus, R. MacDowall, D. C. Folta, A. Mandell, C. Brambora, D. Patel, S. Banks, K. Hohman, V. Hruby, K. Brown, J. Kruth, and R. Cox, "Lunar Ice Cube: Determining Volatile Systematics Via Lunar Orbiting Cubesat," *European Planetary Science Congress*, Vol. 10, Oct 2015, pp. EPSC2015–61.

[4] A. J. Mazarr and D. C. Folta, "Low-Thrust Station-Keeping for a Highly Elliptical Polar Orbit at the Moon," *AAS/AIAA Astrodynamics Specialist Conference*, Snowbird, Utah, 2018, pp. 1–31.

[5] Busek Space Propulsion and Systems, *BIT-3 RF Ion Thruster*, 2019.

[6] C. Russell and C. Raymond, eds., *The Dawn Mission to Minor Planets 4 Vesta and 1 Ceres*. New York: Springer-Verlag, 1 ed., 2012, 10.1007/978-1-4614-4903-4.

[7] R. Mathur, "Low Thrust Trajectory Design and Optimization: Case Study of a Lunar CubeSat Mission," *6th International Conference on Astrodynamics Tools and Techniques*, Darmstadt, Germany, Emergent Space Technologies, Inc., 2016, pp. 1–11.

[8] N. Bosanac, *Leveraging Natural Dynamical Structures to Explore Multi-Body Systems*. PhD thesis, Purdue University, 2016.

[9] N. Bosanac, A. D. Cox, K. C. Howell, and D. C. Folta, "Trajectory Design for a Cislunar Cubesat Leveraging Dynamical Systems Techniques: The Lunar IceCube Mission," *27th AAS/AIAA Space Flight Mechanics Meeting*, San Antonio, Texas, February 2017.

[10] N. Bosanac, A. D. Cox, K. C. Howell, and D. C. Folta, "Trajectory design for a cislunar CubeSat leveraging dynamical systems techniques: The Lunar IceCube mission," *Acta Astronautica*, Vol. 144, 2018, pp. 283–296, 10.1016/j.actaastro.2017.12.025.

[11] D. C. Folta, N. Bosanac, A. D. Cox, and K. C. Howell, "The lunar icecube mission design: Construction of feasible transfer trajectories with a constrained departure," *Advances in the Astronautical Sciences*, Vol. 158, 2016, pp. 1369–1387.

[12] K. K. Boudad, "Disposal Dynamics From The Vicinity Of Near Rectilinear Halo Orbits In The Earth-Moon-Sun System," Master's thesis, Purdue University, 2018.

[13] D. J. Grebow and T. A. Pavlak, "MColl: Monte Collocation Trajectory Design Tool," *AAS/AIAA Astrodynamics Specialist Conference*, Stevenson, Washington, 2017.

[14] R. E. Pritchett, K. C. Howell, and D. J. Grebow, "Low-Thrust Transfer Design Based on Collocation Techniques: Applications in the Restricted Three-Body Problem," *AAS/AIAA Astrodynamics Specialist Conference*, Stevenson, Washington, 2017.

[15] R. E. Pritchett, E. Zimovan, and K. C. Howell, "Impulsive and Low-Thrust Transfer Design Between Stable and Nearly-Stable Periodic Orbits in the Restricted Problem," *2018 AIAA/AAS Space Flight Mechanics Meeting*, Orlando, Florida, 2018, 10.2514/6.2018-1690.

[16] R. Pritchett, A. D. Cox, K. C. Howell, D. C. Folta, and D. Grebow, "Low-Thrust Trajectory Design Via Direct Transcription Leveraging Structures from the Low-Thrust Restricted Problem," *69th International Astronautical Congress*, Bremen, Germany, 2018, pp. 1–16.

[17] G. Shakhnarovich, P. Indyk, and T. Darrell, "Introduction," *Nearest-Neighbor Methods in Learning and Vision*, ch. 1, pp. 1–12, Cambridge, Massachusetts: MIT Press, 1 ed., 2005.

[18] K. L. Clarkson, "Nearest-Neighbor Searching and Metric Space Dimensions," *Nearest-Neighbor Methods in Learning and Vision*, ch. 2, pp. 15–59, Cambridge, Massachusetts: MIT Press, 1 ed., 2005, 10.7551/mitpress/4908.003.0005.

[19] M. Vaquero and J. Senent, "Poincare : A Multi-Body, Multi-System Trajectory Design Tool," *7th International Conference on Astrodynamics Tools and Techniques*, Oberpfaffenhofen, Germany, 2018, pp. 1–12.

[20] R. D. Falck, N. Glenn, and J. W. Dankanich, "Optimization of Low-Thrust Spiral Trajectories by Collocation," *AIAA/AAS Astrodynamics Specialist Conference*, Minneapolis, Minnesota, 2012, pp. 1–17.

[21] Z. P. Olikara, "Framework for Optimizing Many-Revolution Low-Thrust Transfers," *AAS Astrodynamics Specialists Conference*, Snowbird, Utah, 2018, pp. 1–19.